

INVESTIGATIONS ON THE TURBULENT WAKE VORTEX FLOW OF LARGE TRANSPORT AIRCRAFT

Christian Breitsamter, Claudio Bellastrada and Boris Laschka
Institute for Fluid Mechanics, Technische Universität München
Boltzmannstrasse 15, 85748 Garching, Germany

Keywords: Wake Vortex, Unsteady/Turbulent Flow, Hot-wire anemometry, Large Transport Aircraft

Abstract

The wake vortex formation and development behind a four-engined large transport aircraft model is studied in detail. Wind tunnel experiments have been conducted on an 1:22.5 scaled half-model in landing configuration at a Reynolds number of 0.47×10^6 and at angle of attack of 9.5 deg. The wake flowfield is carefully surveyed at six cross-flow planes located over a distance of 6 wing spans using advanced hot-wire anemometry. The results obtained include distributions of velocity, vorticity and Reynolds stress components. Velocity spectra are also analyzed. The wake vortical structures are characterized by axial vorticity peaks, axial velocity deficits and increased turbulence intensities. Six main vortical structures dominate the wake near field, namely the wing tip vortex, the outboard flap edge vortex, the inboard and outboard nacelle vortices, and the vortices shed at the wing-body junction and the horizontal stabilizer. The outboard flap edge vortex is the strongest vortical structure acting as the roll-up center. Merging with the outboard nacelle vortex and the wing tip vortex is almost completed at 6 span dimensions downstream. Vortex merging due to elliptic instability takes place when a critical ratio of core radius to vortex separation distance of about 0.2 is reached. Velocity spectra taken at flap and wing tip vortices exhibit

peaks attributed to specific inherent instability mechanisms whereas vortex meandering is regarded as a broadband turbulence phenomenon.

Nomenclature

A_R	Aspect ratio
b	Wing span, [m]
b_0	Spacing of rolled-up vortex, sb , [m]
c_L	Lift coefficient, $2LA_R/(\rho U_\infty^2 b^2)$
d	Vortex separation, [m]
f	Frequency, [1/s]
k	Reduced frequency, $f(b/2)/U_\infty$
L	Lift, [N]
l_μ	Wing mean aerodynamic chord, [m]
Re_{l_μ}	Reynolds number, $U_\infty l_\mu/\nu$
r_1	Viscous vortex core radius, [m]
r_2	External vortex core radius, [m]
$S_{u'}^N$	Power spectral density of u' normalized with $(\Delta k U_\infty)/(\overline{u'^2}(b/2))$
s	Spanwise load factor, Γ/Γ_0
t	Time, [s]
t^*	Non-dimensional time
U_∞	Freestream velocity, [m/s]
u, v, w	Streamwise, lateral and vertical velocity, [m/s]
$\bar{u}, \bar{v}, \bar{w}$	Streamwise, lateral and vertical mean velocity, [m/s]
u', v', w'	fluctuation part of u, v, w , [m/s]
x^*, y^*, z^*	Non-dimensional distances in axial, lateral and vertical direction, $x^* = x/b, y^* = y/(b/2), z^* = z/(b/2)$
Γ, Γ_0	Circulation, Root circulation, [m^2/s]
λ	Wavelength, [m]

Copyright © 2002 by C. Breitsamter, C. Bellastrada and B. Laschka. Published by the International Council of the Aeronautical Sciences, with permission.

ν	Kinematic viscosity, $[m^2/s]$
$\bar{\omega}_x$	Mean axial vorticity component, $(d\bar{v}/dy - d\bar{v}/dz)$, $[1/s]$
ρ	Density, $[kg/m^3]$
ξ	Non-dimensional axial vorticity component, $\bar{\omega}_x(b/2)/U_\infty$

1 Introduction

Wake vortices emanating from Large Transport Aircraft (LTA) may endanger the flight safety of a following aircraft encountering the wake [14]. In the past the wake vortical structure and related issues have been intensively investigated [13]. It is well known that the trailing wake of a lifting body rolls up into a pair of strong counter-rotating longitudinal vortices that persists for many body dimensions downstream. The vortex strength is proportional to the bound circulation or body lift, and hence, for steady flight conditions this is approximately proportional to the weight of the generating aircraft. An aircraft encountering a vortex wake can experience sudden upwash, downwash or rolling along with increased structural loads, depending on its position and orientation with respect to the wake. Near the ground this can be especially dangerous, as the pilot has less time to recover from rapid changes in the aircraft's attitude.

Up to now flight safety has been ensured by maintaining a suitably large spacing between the aircraft during take-off and landing, as well as on flight routes [3]. The Federal Aviation Administration in the U.S. and Civil Aviation Authority in Europe regulate the separation distances. These distances are often overly conservative to account for the varying behaviour of the vortices under different atmospheric conditions [12]. In particular, wake vortices of the future generation of Very Large Transport Aircraft (VLTA), beyond the size of 747-class jets, are of major concern as VLTA aircraft weights does not fit in existing separation rules, and enlarging the aircraft spacing would hamper significantly an efficient VLTA operation. Consequently, there is a strong demand on developing a means of tracking or eliminating the trailing vortex hazard [5], [12].

Precise tracking or prediction of wake vortex

locations under all weather conditions is beyond the range of current technology. Therefore, many research activities concentrate on alleviating the wake vortex hazard by modifications of wing geometry and/or wing loading. Strategies to minimise the wake vortex hazard concentrate either on a Low Vorticity Vortex (LVV) design or on a Quickly Decaying Vortex (QDV) [12]. The LVV design reduces the wake vortex hazard by enhancing the diffusion of the vorticity field. It is aimed on the generation of wake vortices with larger core size and smaller swirl velocities at the core radius after roll-up is completed. Also, an optimum wing load distribution may minimise the induced rolling moment for a following aircraft. The alteration of the circulation distribution of the wake generating wing can be obtained by using differential flap settings. It has been shown that a wing with an outboard partially deflected flap and an inboard fully deflected flap produces, at least in the near field, a smaller induced rolling moment than a wing with a standard flap setting [4]. An enhanced vortex decay may be achieved by promoting three-dimensional instabilities by means of active or passive devices [20], [21], [22]. An active system tested by Boeing uses periodic oscillations of control surfaces to introduce the desired perturbations leading, after sufficient amplification, to the breakup of the vortices into vortex rings [7]. Since a multiple-vortex system shows instabilities which can grow more rapidly, passive devices aim to promote this kind of instabilities through the deliberate production of single vortices in addition to those coming from the wing tip and the flap edge [20], [10]. The efficiency of these concepts depends on the persistence of separate vortex pairs which is determined by configurational details of the aircraft wing [23].

While the origin of wake turbulence is generally recognised, its physical characteristics in space and time are still not completely understood. To fill this gap a Critical Technology Project on Wake Vortex Characterisation and Control, named C-Wake, has been started within the 5th Framework Program of the European Community (EC) [15]. The wake vortex characteristics are studied using various experimental and

numerical methods [5]. Tests are conducted on generic models as well as on detailed LTA and VLTA models. Wind tunnel, towing tank and catapult experiments give specific and complementary data resulting in a better description of the vortical structures of the different wake regions. Further, flight tests have been performed using triangular lidar measurements to observe and reveal the development of an aircraft generated wake under real meteorological conditions [11]. Also, several computational methods are used to provide reasonable estimates of the length of the hazardous wake vortex region [5]. The vortex models employed depend strongly on the treatment of turbulent and unsteady quantities. Recent experimental studies have shown the importance of unsteady effects on the wake vortex formation and evolution [1], [17], [18]. Therefore, the Institute for Fluid Mechanics (FLM) of the Technische Universität München (TUM) is involved in the C-Wake project by investigating the turbulent and unsteady wake vortex flow structure subject to a typical E4-type LTA model. The results presented herein focus on axial velocity and vorticity distributions complemented by Reynolds shear stress patterns and spectral densities.

2 Test Technique and Test Program

2.1 Description of Model and Facility

The experiments were performed on a detailed rigid stainless steel half-model of a typical E4-type LTA. The model scale is 1:22.5 corresponding to a wing half-span of 1.301 m, a wing mean aerodynamic chord of 0.323 m and a fuselage length of 2.605 m. The wing has sets of fully deployable flaps, ailerons and slats to study take-off and landing configurations. Further, the model is equipped with two through-flow nacelles. Two strakes are mounted on the inboard nacelle and one strake on the outboard nacelle. Landing gear and vertical tail plane are not installed.

The tests were carried out in the FLM low-speed wind tunnel facility C. This facility featuring a closed test section with a height of 1.8 m, a width of 2.7 m and a length of 21 m is de-

signed and usually employed for civil aerodynamics investigations. Maximum usable velocity is 30 m/s with a turbulence level less than 0.5%. Also, the long range test section is ideally suited to conduct wake vortex measurements. With the model in place the pressure gradient along the test section's streamwise (axial) direction was set to zero by slightly increasing downstream the test section height by means of an adjustable ceiling. The model is positioned on the tunnel floor with the reference point 2.6 m downstream of the nozzle exit and the wing tip pointing upwards (Fig. 1). A peniche of 0.095 m height is used to raise the model fuselage above the wind tunnel floor boundary layer. The model wing box is attached to the driven shaft of a computer-controlled model support located below the test section floor, allowing a precise angle-of-attack setting. The test section is further equipped with a three-degree-of-freedom probe traversing system giving minimum steps of ± 0.2 mm in axial, lateral and vertical directions.

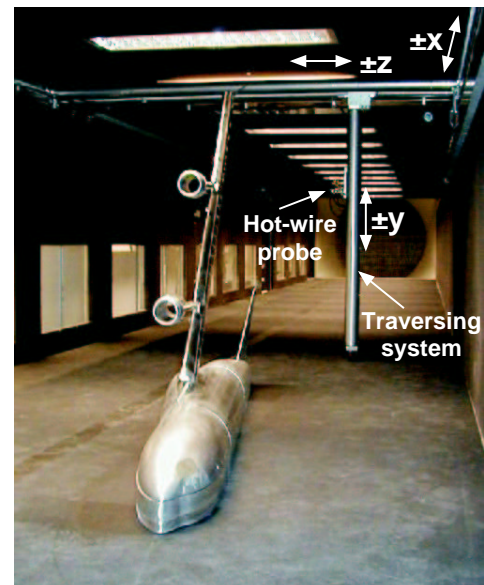


Fig. 1 LTA E4-type half model mounted in long range test section of FLM wind tunnel C.

2.2 Measurement of Unsteady Velocities

Sophisticated triple-sensor hot-wire probes were used to measure the instantaneous flowfield velocities. The sensors consist of 5- μ m-diam. plat-

inert-plated tungsten wires giving a length/diameter ratio of 250. The measuring volume formed by the wires is approximately 1 mm in diameter. The wires are arranged perpendicular to each other to achieve best angular resolution [2]. An additional temperature probe is employed to correct anemometer output-voltages if ambient flow temperature varies.

The hot-wire probes were operated by a multi-channel constant-temperature anemometer system. By means of its signal conditioner modules, bridge output voltages were low-pass filtered at 820 Hz before digitization and amplified for optimal signal level. The signals were then digitized with 16-bit precision through the sixteen-channel simultaneous-sampling A/D converter of the PC high-speed board. The sampling rate for each channel was set to 3000 Hz giving a Nyquist frequency of 1500 Hz. The sampling time was 6.4 s resulting in a sample block of 19200 values for each survey point. The sampling parameters were achieved by preliminary tests to ensure that all significant flowfield phenomena are detected. Each digitized and temperature corrected voltage triple was converted to calculate the time-dependent velocity components u , v , and w . The numerical method used is based on look-up tables derived from the full velocity and flow angle calibration of the sensors [2]. Statistical accuracy of the calculated quantities was considered as well. Random error calculations gave accuracies of 0.5, 2, and 3.5% for the mean and standard deviation and spectral density estimation, respectively [2].

Regarding the susceptibility of vortical structures to intrusive measurements, it was found that the presence of the probe has no markable influence on the wake vortex formation and evolution. Especially, vortex meandering is not significantly modified [17].

2.3 Test Conditions

For the tests reported herein, a high-lift landing configuration is studied with the inboard, mid-board and outboard slats set at 19.6°, 23.0°, and 26.5°, respectively, both inboard and outboard

flaps set at 26.0°, and the aileron set at 10°. The horizontal tailplane is fixed at -9.5° while the angle of attack is set to 9.5° related to a lift coefficient of $c_L = 1.76$. The experiments were made at a freestream reference velocity of $U_\infty = 25 \text{ m/s}$ corresponding to a Reynolds number of $Re_{l_\mu} = 0.471 \times 10^6$. Transition strips are carefully put on the wing nose section to avoid any laminar separation. Inspecting the surface flow by tufts it was proven that attached flow is present on wing and control surfaces (Fig. 2).

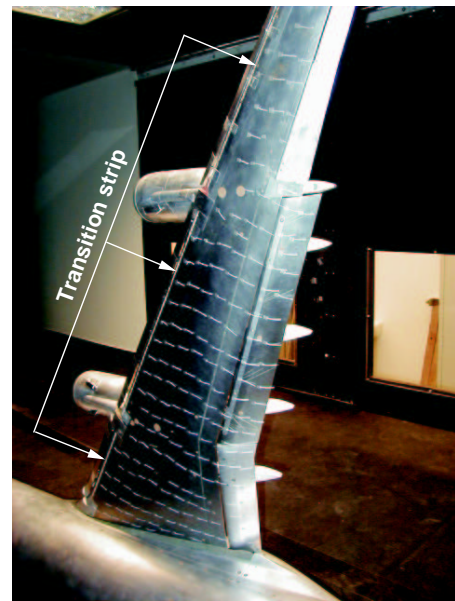


Fig. 2 Surface flow visualization using tufts.

The velocity fields downstream of the model were measured in planes perpendicular to the freestream direction at six distances relative to the wing tip trailing edge ranging from $x/b = x^* = 0.37 \div 5.56$ (Tab.1). The survey points are closely spaced in the wake vortex areas known from previous tests with a relative grid resolution of 0.006 in spanwise and 0.004 in vertical direction based on the wing span. Outside these areas a relative grid resolution of 0.035 in spanwise and 0.023 in vertical direction was used. Considering the downstream development a vortex wake can be divided in four regions: (i) the near field, $x/l_\mu = O(1)$, which is characterized by the formation of highly concentrated vortices shed at all surface discontinuities; (ii) the extended near field, $x^* \leq 10$, where the wake roll-up process takes

place, and the merging of dominant vortices (flap edge, wing tip) occurs, leading gradually to two counter-rotating vortices; the far field, $10 \leq x^* \leq 100$, where the wake is descending in the atmosphere and linear instabilities emerge; (iv) the dispersion region, $x^* > 100$, where fully developed instabilities cause a strong interaction between the two vortices until they collapse. However, comparing different experimental results the parameter x^* can only be used unambiguously to describe the wake vortex evolution if the term $c_L/(s^3 A_R)$ is constant. Therefore, an appropriate parameter related to the wake vortex age is given by the non-dimensional time t^* which takes the spanwise load factor s into account [12].

$$t^* = x^* \frac{c_L}{4\pi s^3 A_R} \quad (1)$$

A typical value for an elliptical loaded wing is $s = \pi/4$, whereas for a high-lift configuration s may deviate from $\pi/4$. Here, $s = \pi/4$, $c_L = 1.76$, and $A_R = 9.302$ are used. [1]. The values of x^* and t^* referring to the position of the measurement planes, and the values of y^* and z^* describing their spanwise and vertical extensions, are collected in Table 1. It can be seen from the table that the following results concern the wake vortex formation and evolution in the near field and extended near field with a maximum vortex age of $t^* = 0.173$.

Plane	t^*	x^*	y^*	z^*
4	0.011	0.37	$0 \div 1.10$	$0 \div 0.76$
9	0.031	1.00	$0 \div 1.10$	$0 \div 0.90$
11	0.062	2.00	$0 \div 1.10$	$0 \div 0.90$
13	0.093	3.00	$0 \div 1.10$	$0 \div 0.90$
13a	0.124	4.00	$0 \div 1.10$	$0 \div 0.90$
15	0.173	5.56	$0 \div 1.10$	$0 \div 0.90$

Table 1 Position and size of measurement planes.

3 Results and Discussion

3.1 Mean Axial Vorticity and Velocity Fields

The three-dimensional flowfield of the model wake is documented in the six cross flow planes both by contours of normalized axial vorticities

ξ (Figs. 3 and 4) and streamwise (axial) velocities \bar{u}/U_∞ (Fig. 6). The axial vorticity is used as the main quantity to identify significant vortical structures and to define their location on each cross flow plane. The vorticity contents of the thin shear layer originating from the wing trailing edge is mainly determined by a change in the direction of the velocity vector across the trailing edge, and not by the vorticity already present within the boundary layers passing the trailing edge. Consequently, the interaction between the vorticity field and the velocity and pressure distribution on the wing will be weak, and the orientation of the vorticity vector is approximately perpendicular to the trailing edge [13]. In the near field at $x^* = 0.37$, the formation of distributed vortical structures is observed (Figs. 3, 4a). Among these structures high levels of peak vorticity indicate six dominant vortices: the wing tip vortex (WTV), the outboard flap edge vortex (OFV), the outboard and inboard nacelle vortices (ONV and INV), the vortex emanating from the wing-fuselage junction (WFV) and the horizontal tail tip vortex (HTV). Except the HTV, all these vortices are embedded in the wing vortex sheet. The WTV is characterized by a high peak of positive vorticity ($\xi = 37$) resulting from vorticity generated at the winglet, and vorticity shed at the wing tip and winglet junction. The OFV and ONV, located approximately in-line with the outboard engine nacelle and the outer edge of the outboard flap, contain vorticity of the same sign with peaks of $\xi = 39$ and $\xi = 15$, respectively. The comparison of all peak vorticity values shows that the OFV is the strongest vortical structure in the wake. The weaker ONV is attributed to the rolled-up shear layer of the outboard through-flow nacelle and the nacelle strake. The INV exhibits a much stronger vorticity peak than the ONV because the inboard nacelle has two strakes while the outboard nacelle has only one. Measurements performed in the DNW-LLF wind tunnel show the same behaviour of outboard and inboard nacelle vortices [16]. Note that for a powered aircraft the jet-vortex interaction must also be taken into account. The two remaining vortices of significant strength are both characterized

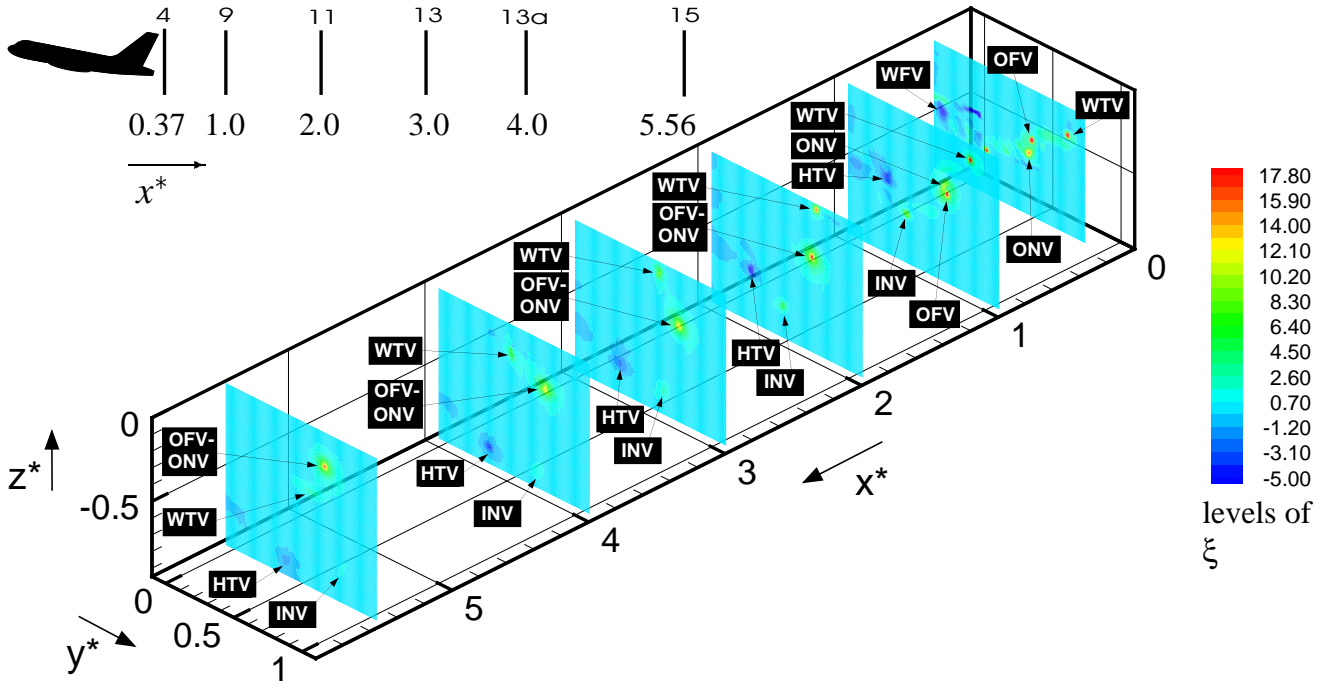
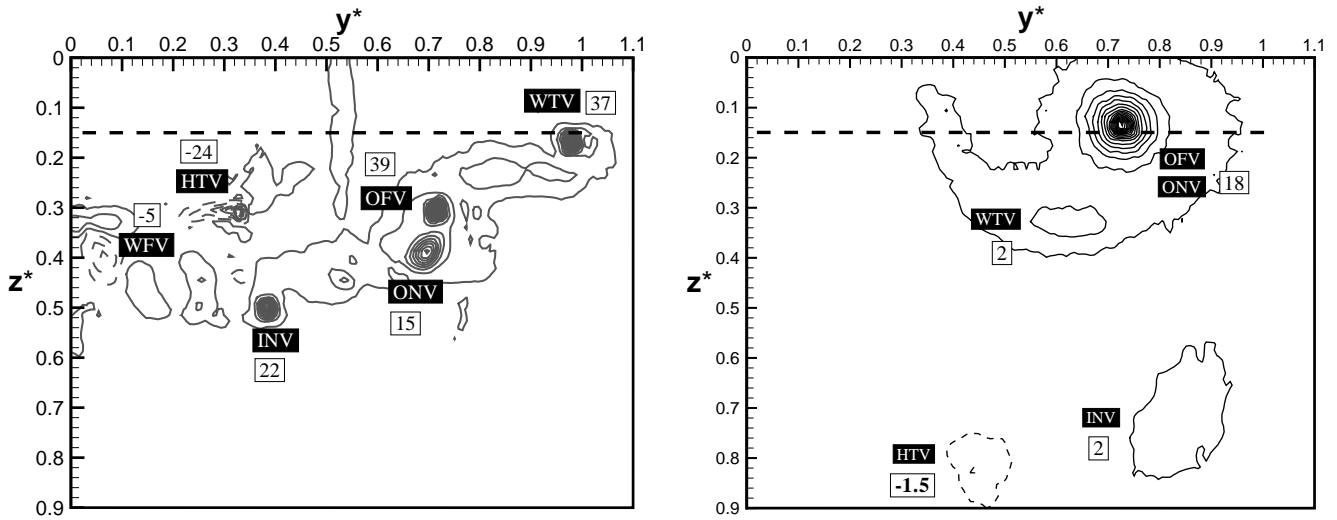


Fig. 3 Non-dimensional axial vorticity distributions ξ for all cross flow planes investigated.



a) $x^* = 0.37$ (Plane 4)

b) $x^* = 5.56$ (Plane 15)

Fig. 4 Non-dimensional axial vorticity distributions ξ at $x^* = 0.37$ and $x^* = 5.56$. The dashed line refers to the wing trailing-edge position. Vorticity peaks are marked by numbers.

by peaks of negative vorticity, namely $\xi = -5$ for the WFV and $\xi = -24$ for the HTV. Focusing on the WFV region a substantial amount of negative vorticity is also generated at the inboard flap edge. The HTV is located above the wing vortex sheet and fully separated from the descending wing vortex layer. The horizontal tail was set at an incidence of -9.5° , thus producing negative lift corresponding to a tip vortex of negative vor-

ticity. Also, several vortical structures of less strength can be detected, attributed e.g. to aileron gap, flap track fairings, and slat edges.

At $x^* = 1.0$, the ONV is nearly completely merged with the stronger OFV. A plateau in the function of the ONV axial peak vorticity versus streamwise distance indicates the merging of the OFV and ONV (Fig. 5). The OFV-ONV system then becomes the roll-up centre of the whole vor-

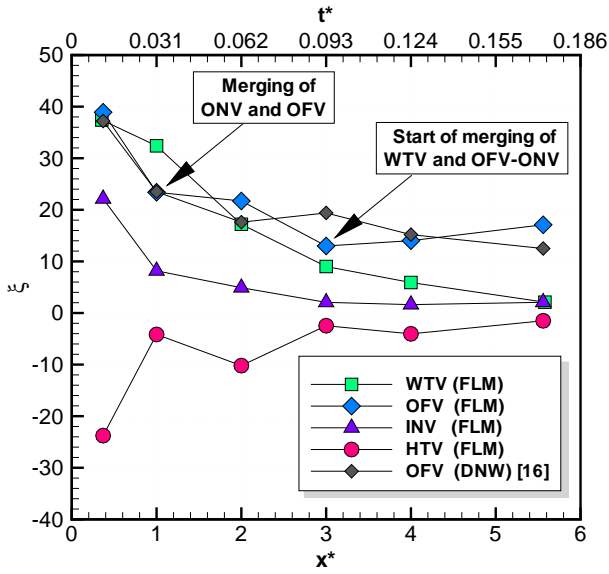


Fig. 5 Non-dimensional axial peak vorticities ξ as function of x^* for various dominant vortices.

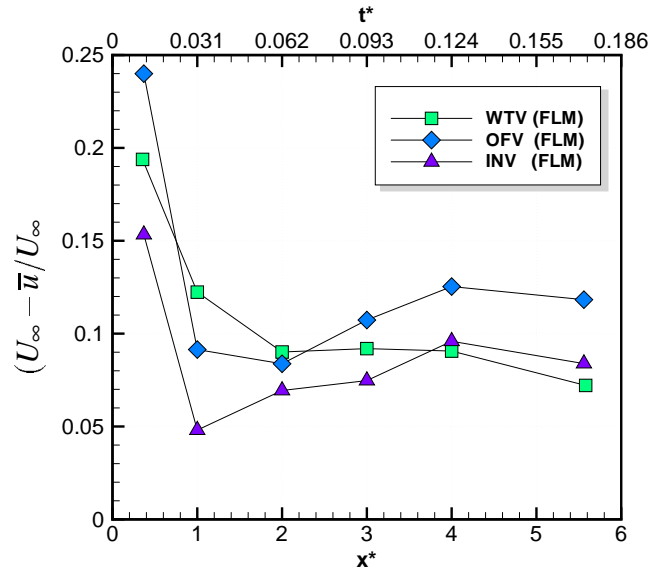


Fig. 7 Axial velocity deficits $(U_\infty - \bar{u})/U_\infty$ of vortex cores as function of x^* for various dominant vortices.

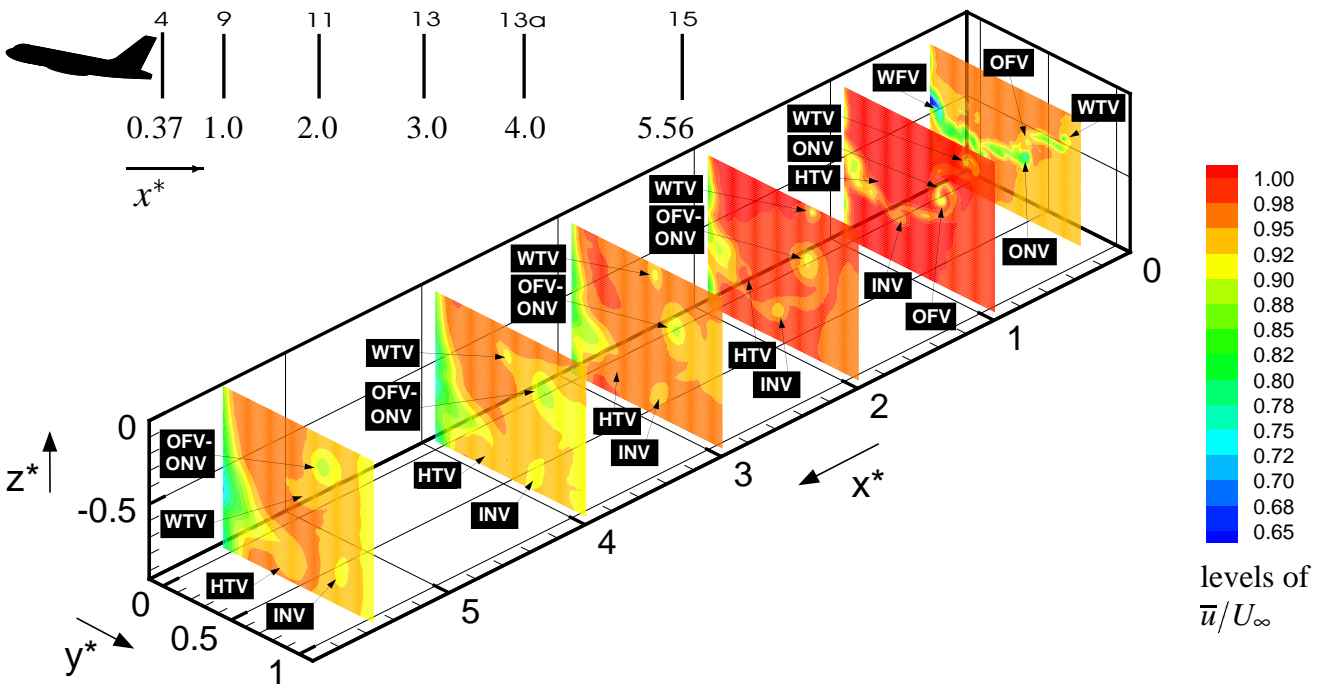


Fig. 6 Non-dimensional axial velocity distributions \bar{u}/U_∞ for all cross flow planes investigated.

text sheet, all other vortices are seen to be rotating counterclockwise around it. Due to the induced velocity field of the OFV–ONV system the WTV is moved upward and inboard while HTV, WFV and INV are moved downward. At $x^* = 2.0$, a further merging process between negative vorticity areas surrounding the HTV takes place, evident

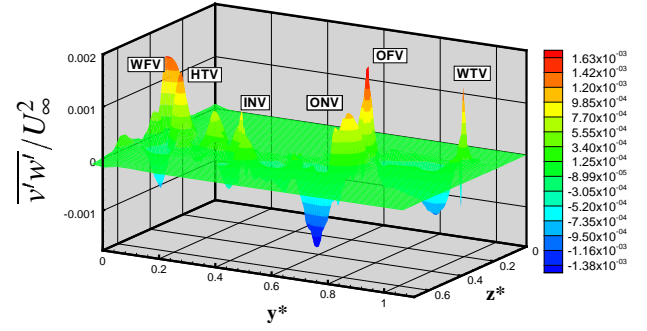
by an increase in the negative peak vorticity of the HTV (Fig. 5). At $x^* = 3.0$, the dominant OFV–ONV system starts to incorporate the WTV, the strength of which has been reduced since $x^* = 2.0$ (Fig. 3). The peak vorticity of the INV, still entirely separated from the main vortex system, is also reduced. Downstream, the vorticity of the WTV is continuously fed into the stronger OFV–ONV, and hence this vortex system increases in strength (Fig. 5). At $x^* = 5.56$, the merging of

the WTV and the dominant OFV–ONV system is almost completed (Fig. 4b). The INV and the HTV continue to move counterclockwise around the rolled-up vortex system. At this stage, no merging of these vortices with the OFV–ONV system is observed. The spanwise load factor $s = b_0/b \approx 0.71$ calculated from the measured spacing b_0 of the rolled-up vortex system matches very close the theoretical value for the elliptical loaded wing, $s = \pi/4$, thus substantiating the values given in Sec. 2.3.

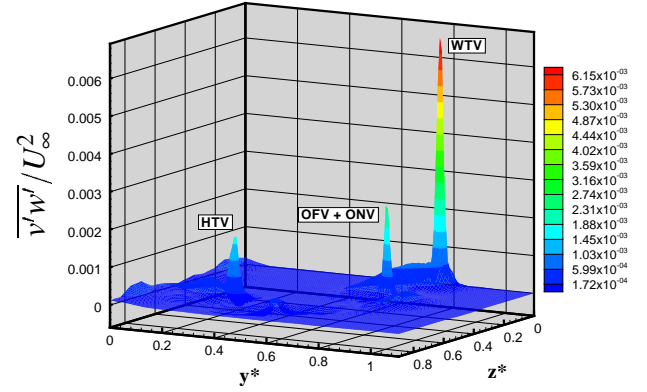
Considering the axial velocity distribution the trailing vortices are usually found to be of the wake type, i.e. with an axial core velocity smaller than the freestream velocity (Fig. 6). The downstream development of the axial velocity deficit $(U_\infty - \bar{u})/U_\infty$ taken at the centre of the dominant vortical structures is plotted in Fig. 7. At $x^* = 0.37$, the deficit at the cores of the WTV and OFV are 19% and 24%, respectively. From $x^* = 0.37$ to $x^* = 1.0$, a strong decrease in the axial velocity deficit is detected before further downstream, after vortices have merged, the velocity deficit increases again. At the most downstream station, the velocity defect stabilises at approximately 7% for the vanishing WTV and 12% for the rolled-up OFV system. These values are considerable because they are in the range of 25% ÷ 30% of the maximum tangential velocities. Consequently, the wake type profiles of the axial core velocities are important for wake vortex models and the evolution of instability mechanisms.

3.2 Reynolds Stress Patterns

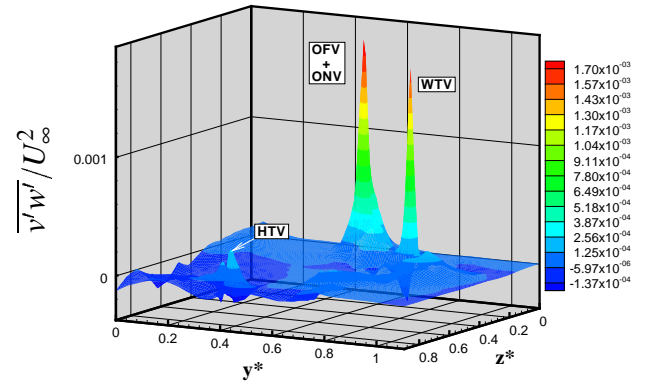
Reynolds normal and shear stress components are computed from the velocity fluctuations and typically normalized by the square of the freestream velocity. Here, carpet plots of the Reynolds shear stress component $\overline{v'w'}/U_\infty^2$ are presented, since it concerns the fluctuations of the velocity components defining with their spatial gradients the axial rotation (Fig. 8). At $x^* = 0.37$, dominant vortical structures are marked by turbulent shear stress peaks of opposite sign, the vortex centres are indicated by the position where the shear stress changes sign. A comparison of vor-



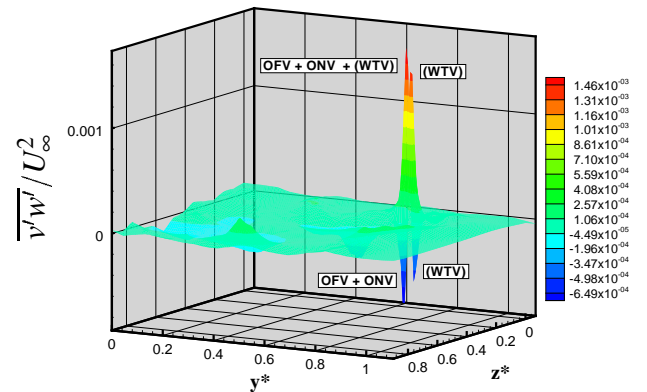
a) $x^* = 0.37$ (Plane 4)



b) $x^* = 2.00$ (Plane 11)



c) $x^* = 4.00$ (Plane 13A)



d) $x^* = 5.56$ (Plane 15)

Fig. 8 Carpet plots of Reynolds shear stresses $\overline{v'w'}/U_\infty^2$ at stations $x^* = 0.37, 2.0, 4.0,$ and 5.56 .

tex centre positions determined in this way with those identified by the axial vorticity peaks shows good agreement (Fig. 8a and Fig. 4a). While the dominant vortices are manifested by very sharp peaks of turbulent shear stress, the wing vortex sheet including vortical structures of less energy exhibit smoother distributions. The distinct peaks of turbulent shear stresses can be used to provide information on the vortex core regions. The analysis points out that the viscous core radius, e.g for WTV and OFV, is of the order of $r_1 \approx 0.01 b$, whereas the external core radius defined by the region including nearly the total amount of vorticity or circulation of the vortex is of the order of $r_2 \approx 0.1 b$. A similar scaling is reported in [17]. At $x^* = 2.0$, high peaks of turbulent shear stresses are still attributed to the WTV, the OFV–ONV system, and the HTV (Fig. 8b). The merging of the OFV–ONV system with the WTV during the roll–up process is also documented by studying the change in the related turbulent shear stress peaks, along with the turbulent shear stress distribution between these vortical structures (Figs. 8c, 8d). A double peak of turbulent shear stresses of opposite sign at $x^* = 5.56$ represents the close location of WTV and OFV–ONV, demonstrating that merging of the WTV with the OFV–ONV system is nearly completed.

3.3 Unsteady Effects

3.3.1 Vortex Merging

Experimental and numerical studies have shown that at high Reynolds numbers ($Re \geq 10^4$) three-dimensional (3D) vortex merging is linked to a short wave elliptic instability [18]. In comparison to the two-dimensional case, the 3D merging leads to an earlier merging, and results in a final vortex of higher turbulence intensity and of larger core size. The instability is sensitive to the strain effect mutually evoked by two closely spaced vortices on each other, and this strain is augmented as the vortex spacing decreases. An empirical criterion has been formulated for the 3D merging process based on a critical ratio of (external) core radius to vortex distance of $r_2/d \approx 0.2 \div 0.25$. This value is reached through the

decrease of d due to the roll–up of the vorticity sheets while r_2 remains nearly constant. Typically, the number of revolutions before merging is approximately $1 \div 2$. The 3D merging criterion is proven herein by analyzing the merging process of the ONV with the OFV, and the WTV with the OFV–ONV system. Values of r_2/d are given in Fig. 9, which depicts turbulence intensity distributions $\sqrt{\overline{w'^2}}/U_\infty$ at various downstream stations for the areas where vortex merging takes place. While the vortex core regions show levels of maximum turbulence intensity the vorticity sheets are marked by clearly lower levels. It is demonstrated that the merging criterion holds for both cases under consideration.

3.3.2 Vortex Instabilities

Power spectral densities of axial velocity fluctuations taken at WTV and OFV core regions at $x^* = 5.56$ are evaluated to detect spectral peaks associated with specific instability mechanisms (Fig. 10). The spectral densities are calculated using linear band averaging with 1024 frequency bands. The spectra exhibit dominant reduced frequencies for the WTV at $k_{d1-4} = 0.38, 0.84, 1.92,$ and 4.04 and for the OFV at $k_{d1-4} = 0.36, 0.65, 1.62,$ and 2.78 , indicating that turbulent kinetic energy is channeled into a narrow band driven by quasi-periodic fluctuations.

The presence of instability mechanisms propagating along the wake vortex in streamwise direction can lead to a relevant distortion of the vortex, accelerating its decay and dispersion. Usually, long and short wave instabilities occur. The most significant long wave instability for a vortex pair is the Crow instability [8]. This instability is related to the strain effect induced by one vortex of a pair on the other one, and appears as a sinusoidal displacement of the vortices; it is ultimately responsible for the wake vortex collapse in the far field. Regarding two vortex pairs Crouch observed an instability mechanism with both symmetric and asymmetric modes, the wavelengths of which are shorter than those of the Crow instability, but large with respect to the effective vortex core size [6]. A Crouch type insta-

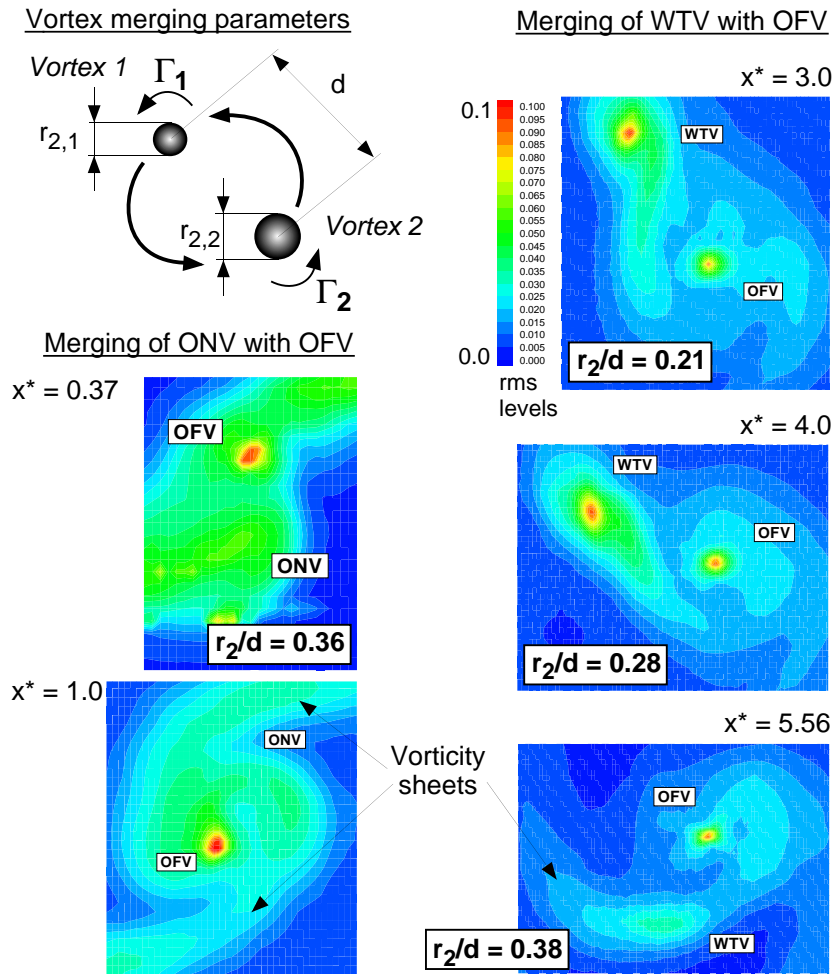


Fig. 9 Vertical turbulence intensity distributions $\sqrt{w'^2}/U_\infty$ indicating the merging of the ONV with the OFV and of the WTV with the OFV; LTA-E4 type high lift configuration, $Re_{l_\mu} = 0.47 \times 10^6$, $\alpha = 9.5^\circ$.

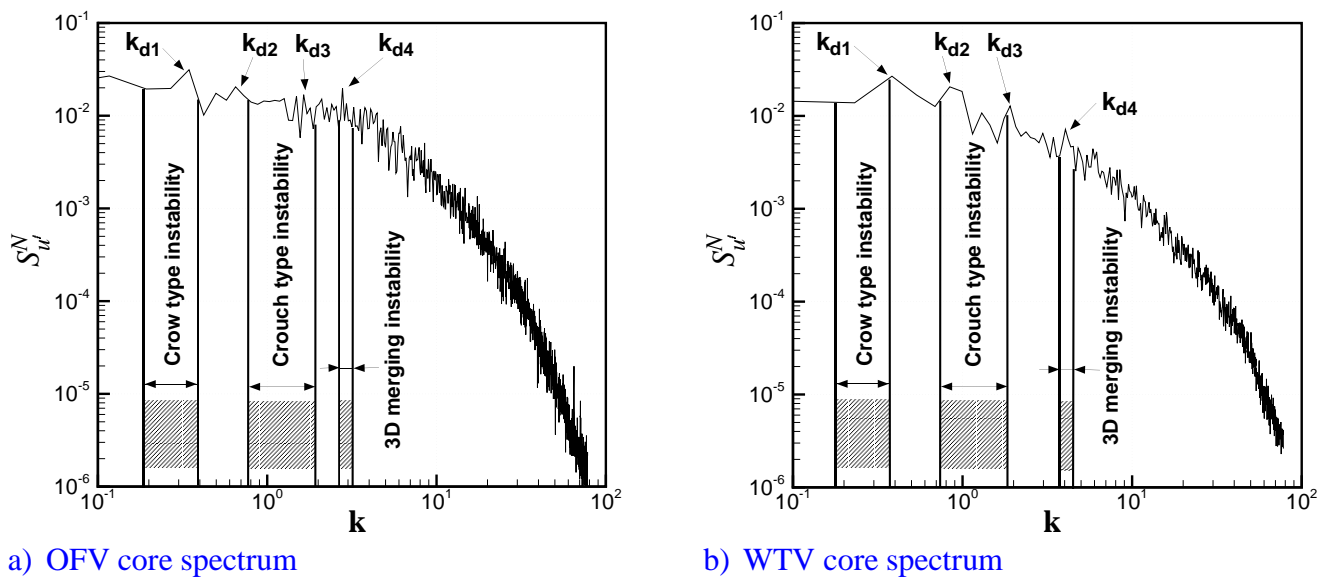


Fig. 10 Normalized power spectral densities of axial velocity fluctuations $S_{u'}^N$ for OFV and WTV core stations at $x^* = 5.56$; LTA-E4 type high lift configuration, $Re_{l_\mu} = 0.47 \times 10^6$, $\alpha = 9.5^\circ$.

bility may enhance wake vortex dispersion within $x^* < 30$ [10]. Wavelengths of Crow and Crouch type instabilities are $\lambda_{Crow} \approx 8b_0$ and $\lambda_{Crouch} \approx 2.5d \div 6d$, respectively (here d denotes the distance between WTV and OFV). For the present case, these wavelengths correspond to reduced frequencies of $k_{Crow} = b/(2\lambda_{Crow}) \approx 0.18$ ($\approx 2k_{d1}$) and $k_{Crouch} = b/(2\lambda_{Crouch}) \approx 0.79 \div 1.89$. It can be seen that the values of $k_{d2,3}$ match with the range of k_{Crouch} emphasizing a Crouch type instability due to the interaction of WTV and OFV.

A typical short wave instability of the Widnall type is characterized by a wavelength of the order of the vortex core size, depending also on the internal vortex core structure ($\lambda_{Widnall} \approx 2 \div 3r_1$) [24]. This instability can also grow in a vortex pair, interfering at the same time with long wave instabilities. The short wave elliptic instability due to the 3D merging has a wavelength of the order of $4r_2$. This type of instability is highlighted by the spectral peaks at k_{d4} . It may also lead to changes in the vortex core structure generating secondary vortex pairs normal to the main vortex pair axes [18]. The formation of such transversal vortex pairs can be responsible for the breakdown of the flow into small scale turbulent motion. This effect becomes enhanced when the elliptic instability interacts with a growing Crow instability.

3.3.3 Vortex Meandering

Vortex meandering can be observed for high Reynolds number vortices in cases of both high lift and cruise configurations, and reveals itself through fluctuations of the vortex core. It is an important unsteady phenomenon which is not yet fully understood. Recent investigations [17] have demonstrated that meandering is not caused by wind tunnel perturbations or wall effects, as stated e.g. in [9]. Vortex meandering may be explained by the propagation of perturbations emanating from the aircraft turbulent vortex sheet, i.e. from the flow surrounding the vortex cores at the very beginning of the roll-up process in the near field [19], [17]. The spectral densities presented substantiate that meandering is due to broadband perturbations sharply localised in the vortex cen-

tres. Therefore, no definite scale is amplified.

4 Conclusions

Comprehensive experimental investigations have been conducted on the formation and evolution of the turbulent wake vortex flow emanating from a 1 : 22.5 scaled half-model of a four-engined large transport aircraft. A typical high-lift landing configuration is studied at angle of attack of 9.5 deg and a Reynolds number of 0.47×10^6 . Advanced hot-wire anemometry is applied to measure the time-dependent velocity fields. Six cross flow planes are inspected located at stations in the range of 0.37 to 5.56 wing spans downstream of the wing tip trailing edge. Consequently, the analysis focuses on the near field and the extended near field. The quantities discussed comprise axial vorticity and velocity fields supplemented by distributions of turbulence intensities and Reynolds shear stresses. Spectral densities are also evaluated. The main results of these investigations are as follows:

1. The wake near field show six significant vortical structures, namely the wing tip vortex (WTV), the outboard flap edge vortex (OFV), the outboard and inboard nacelle vortices (ONV and INV), the vortex emanating from the wing-fuselage junction (WFV) and the horizontal tail tip vortex (HTV). Except the HTV, all vortices are connected through the vortex sheet shed at the wing trailing-edge. In sense of rotation of the WTV, the OFV, ONV and INV are co-rotating vortices whereas WFV and HTV are counter-rotating vortices. The highest level of axial peak vorticity is attributed to the OFV, which is therefore the strongest and most persistent vortical structure in the wake.
2. In the extended near field the position and strength of the vortices change progressively because of the wake roll-up process and vortex merging. At $x^* = 2.0$, OFV and ONV are completely merged, thus creating the dominant vortex system which acts as

the wake roll-up centre. The WTV starts to merge with the OFV-ONV system at $x^* \geq 3.0$, and at the most downstream station $x^* = 5.56$, the roll-up process is nearly completed. A noticeable result is the strength and persistence of the INV which at this station is still separated from the OFV-ONV system.

3. The core regions of the main wake vortices are characterized by axial vorticity peaks and considerable axial velocity defects. The turbulent vortex core structure reveal maximum turbulence intensities and Reynolds shear stress peaks of opposite sign. Progressing downstream the levels of these peak values change due to vortex merging and diffusion. Characteristic dimensions of the vortex core radii are found to be $\leq 0.01 b$ for the viscous core radius and $\approx 0.1 b$ for the external core radius.
4. It has been proven that three-dimensional vortex merging associated with an elliptic short-wave instability occur when a critical ratio of external core radius to vortex separation distance of $r_2/d \approx 0.2 \div 0.25$ is reached.
5. Spectral analysis of the axial velocity fluctuations performed for both the WTV and OFV core regions shows broadband distributions with concentrations of turbulent kinetic energy at reduced frequencies of $k_{d3} \approx 1.6$ (OFV), and 1.9 (WTV) and $k_{d4} \approx 2.8$ (OFV), and 4.0 (WTV). These spectral peaks indicate particularly a Crouch type instability (k_{d3}) and a 3D merging elliptic instability (k_{d4}), while vortex meandering is considered as a broadband turbulence phenomenon with no amplification of a definite scale.

Acknowledgment

This work is part of the C-Wake Critical Technology Project co-funded by the European Union

through the Research Framework Programme under CEC Contract No. G4RD-CT1999-00141 coordinated by Airbus Deutschland GmbH. The authors want to express their appreciations to Dr.-Ing. K. Hünecke and Mrs. Dipl.-Ing. C. Hünecke (Airbus Deutschland, Bremen) for fruitful cooperations.

References

- [1] Bellastrada C, Breitsamter C, and Laschka B. Investigation of Turbulent Wake Vortex Originating from a Large Transport Aircraft in Landing Configuration. *Proc CEAS Aerospace Aerodynamics Research Conference*, pp 31.1–31.10, Cambridge, U.K., June, 2002.
- [2] Breitsamter C. *Turbulente Strömungsstrukturen an Flugzeugkonfigurationen mit Vorderkantenwirbeln*. Dissertation, Technische Universität München, Herbert Utz Verlag (ISBN 3-89675-201-4), 1997.
- [3] Brenner F. Air Traffic Control Procedures for the Avoidance of Wake Vortex Encounters: Today and Future Developments by Deutsche Flugsicherung GmbH. *Proc The Characterisation & Modification of Wakes from Lifting Vehicles in Fluids, AGARD-CP-584*, pp 4-1-4-14, Trondheim, Norway, May, 1996.
- [4] Corsiglia V. R and Dunham R. E. Aircraft wake vortex minimization by use of flaps. *Proc NASA SP-409*, pp 305–338, 1976.
- [5] Coustols E and de Saint-Victor X. Wake Vortex Dynamics: From Characterisation to Control. *Proc 3rd ONERA-DLR Aerospace Symposium, SI-2*, pp 1–14, Paris, France, June, 2001.
- [6] Crouch J. D. Instability and transient growth for two trailing-vortex pairs. *Journal of Fluid Mechanics*, Vol. 350, pp 311–330, 1997.
- [7] Crouch J. D, Miller G, and Spalart P. R. Airplane trailing vortices. *Boeing AERO Magazine*, Vol. April, No 14, pp 1–8, 2001.
- [8] Crow S. C. Stability Theory for a Pair of Trailing Vortices. *AIAA Journal*, Vol. 8, No 12, pp 2172–2179, 1970.
- [9] Devenport W. J, Vogel C. M, and Zsoldos J. S. Flow structure produced by the interaction and merger of a pair of co-rotating wing-tip vor-

- tices. *Journal of Fluid Mechanics*, Vol. 394, pp 357–377, 1999.
- [10] Fabre D and Jacquin L. Stability of a four-vortex aircraft wake model. *Physics of Fluids*, Vol. 12, No 10, pp 4238–4243, 2000.
- [11] Gerz T. Wake vortex prediction and observation: Towards an operational approach. *Proc 3rd ONERA–DLR Aerospace Symposium, S1–3*, pp 1–10, Paris, France, June, 2001.
- [12] Gerz T, Holzäpfel F, and Darracq D. *Aircraft Wake Vortices – A position paper –*. WakeNet – the European Thematic Network on Wake Vortex, 2001.
- [13] Hoeijmakers H. W. M. Vortex Wakes in Aerodynamics. *Proc The Characterisation & Modification of Wakes from Lifting Vehicles in Fluids, AGARD–CP–584*, pp 1–1–1–12, Trondheim, Norway, May, 1996.
- [14] Hünecke K. Structure of a transport aircraft-type near field wake. *Proc The Characterisation & Modification of Wakes from Lifting Vehicles in Fluids, AGARD–CP–584*, pp 5–1–5–9, Trondheim, Norway, May, 1996.
- [15] Hünecke K. Recent developments in wake vortex research – a view from industry. *Proc Conference on Capacity and Wake Vortices*, pp 1–10, London, U.K., Sept., 2001.
- [16] Hünecke K and Schmidt K. *DNW Wind Tunnel Measurement Results*. private communication, 2000.
- [17] Jacquin L, Fabre D, and Geffroy P. The Properties of a Transport Aircraft Wake in the Extended Near Field: an Experimental Study. *Proc 39th Aerospace Sciences Meeting & Exhibit, AIAA Paper 2001–1038*, pp 1–41, Reno (NV), USA, Jan., 2001.
- [18] Leweke T, Meunier P, Laporte F, and Darracq D. Controlled interaction of co-rotating vortices. *Proc 3rd ONERA–DLR Aerospace Symposium, S2–3*, pp 1–10, Paris, France, June, 2001.
- [19] Miyazaki T and Hunt J. C. R. Linear and nonlinear interactions between a columnar vortex and external turbulence. *Journal of Fluid Mechanics*, Vol. 402, pp 349–378, 2000.
- [20] Ortega J. M, Bristol R. L, and Savas O. Wake Alleviation Properties of Triangular-Flapped Wings. *AIAA Journal*, Vol. 40, No 4, pp 709–721, 2002.
- [21] Özger E, Schell I, and Jacob D. On the Structure and Attenuation of an Aircraft Wake. *Journal of Aircraft*, Vol. 38, No 5, pp 878–887, 2001.
- [22] Rennich S. C and Lele S. K. Method for Accelerating the Destruction of Aircraft Wake Vortices. *Journal of Aircraft*, Vol. 36, No 2, pp 398–404, 1999.
- [23] Spalart P. R. Airplane Trailing Vortices. *Annual Review of Fluid Mechanics*, Vol. 30, pp 107–138, 1998.
- [24] Tsai C. Y and Widnall S. E. The instability of short waves on a straight vortex filament in a weak externally imposed strain field. *Journal of Fluid Mechanics*, Vol. 73, pp 721–733, 1976.